

# ***Energy Transfer Between Eigenmodes in Multimodal Atomic Force Microscopy***

*Sangmin An<sup>1,2</sup>, Santiago D. Solares<sup>1,2,3,4</sup>, Sergio Santos<sup>5</sup> and Daniel Ebeling<sup>6</sup>*

<sup>1</sup>Center for Nanoscale Science and Technology, National Institute of Standards and Technology (NIST), Gaithersburg, Maryland 20899, United States

<sup>2</sup>Maryland NanoCenter, University of Maryland, College Park, Maryland 20742, United States

<sup>3</sup>Department of Mechanical Engineering, University of Maryland, College Park, Maryland 20742, United States

<sup>4</sup>Current address: Department of Mechanical and Aerospace Engineering, George Washington University, Washington, DC 20052, United States

<sup>5</sup>Departament de Disseny i Programació de Sistemes Electronics, UPC-Universitat Politècnica de Catalunya, Av. Bases, 61, E-08242 Manresa, Spain

<sup>6</sup>Institute of Applied Physics, Justus Liebig University of Giessen, 35392 Giessen, Germany

\*Email: [ssolares@umd.edu](mailto:ssolares@umd.edu)

Phone: (301) 405-5035

Fax: (301) 314-9477

**ABSTRACT.** We present experimental and computational investigations of tetramodal and pentamodal atomic force microscopy (AFM), respectively, whereby the first four or five flexural eigenmodes of the cantilever are simultaneously excited externally. This leads to six to eight additional observables in the form of amplitude and phase signals, with respect to the monomodal amplitude modulation method. We convert these additional observables into three or four dissipation and virial expressions, and show that these quantities can provide enhanced contrast that would otherwise remain hidden in the original observables. We also show that the complexity of the multimodal impact leads to significant energy transfer between the active eigenmodes, such that the dissipated power for individual eigenmodes may be positive or negative, while the total dissipated power remains positive. These results suggest that the contrast of individual eigenmodes in multifrequency AFM should be not be considered in isolation and that it may be possible to use different eigenfrequencies to probe sample properties that respond to different relaxation times.

**KEYWORDS:**

Multifrequency atomic force microscopy; bimodal; trimodal; multimodal; virial; energy dissipation

## INTRODUCTION

The field of atomic force microscopy (AFM) has rapidly evolved in the past thirty years encompassing nowadays a wide range of modes of operation, characterization methods and highly specialized techniques, which have been developed to manipulate and understand matter at the nanoscale and even at the atomic level [1-10]. A particular demand on the evolution of the atomic force microscope involves tracking the topography of surfaces while *simultaneously* acquiring complimentary information on mechanical, chemical or even subsurface structural information, among others, which has become possible through multifrequency AFM (MF-AFM) techniques [3, 4, 8, 11-17]. The first MF-AFM method was introduced by Rodriguez and Garcia in 2004 [3], who drove the cantilever simultaneously at two eigenmodes, one of which was used for topographical imaging, while the other one was used to map the compositional contrast across the sample. Since then, this powerful approach of AFM that makes use of externally excited higher eigenmodes and augments the number of contrast channels that are sensitive to material properties has grown considerably. Currently there exist validated bimodal [8, 18-20] and trimodal techniques [16, 21], with bimodal methods still comprising by far the majority of multimodal applications. Here we refer to such methods collectively as multimodal AFM (MM-AFM), which represent a subset within MF-AFM. Other versatile MF-AFM methods include band excitation AFM [22, 23] and its combination with amplitude-modulation AFM [14], spectral inversion [4, 13, 24, 25], intermodulation AFM [26, 27], and dual amplitude resonance tracking [28, 29], among others.

In this paper, we present experimental and computational investigations of tetramodal and pentamodal AFM (see Figure 1 for a schematic of the instrumentation), respectively, whereby the first four or five flexural modes of the cantilever are simultaneously excited

externally in a way that six to eight additional observables are acquired in the form of amplitude and phase signals, while the topography is tracked by controlling the fundamental eigenmode through the amplitude modulation method [1]. These six to eight additional observables can also be directly converted into more physically relevant quantities, such as three or four dissipation and virial expressions, which have units of power and energy, respectively. The virial and dissipated power expressions have been used extensively in AFM to map the relative dominance of conservative (average potential energy of the tip-sample spring during impact) and non-conservative (dissipative) tip-sample interactions across the sample, respectively [20, 30-33]. We show that these quantities can provide enhanced contrast that would otherwise remain hidden in the original observables, and that the complexity of the multimodal impact leads to significant energy transfer between the active eigenmodes. We speculate that the larger number of actual observables could enable future applications involving more robust quantification of relevant sample properties such as the Young's modulus, Hamaker constant or dissipative properties, through the development of more sophisticated inversion techniques than those currently in use. The fact that the sample is being simultaneously probed at a large range of frequencies (from  $\approx 70$  kHz to  $\approx 2.3$  MHz in our experiments and from  $\approx 70$  kHz to  $\approx 4$  MHz in our simulations) also suggests that rapid frequency dependent characterization of surfaces whose material properties exhibit multiple relaxation times may become possible in the near future.

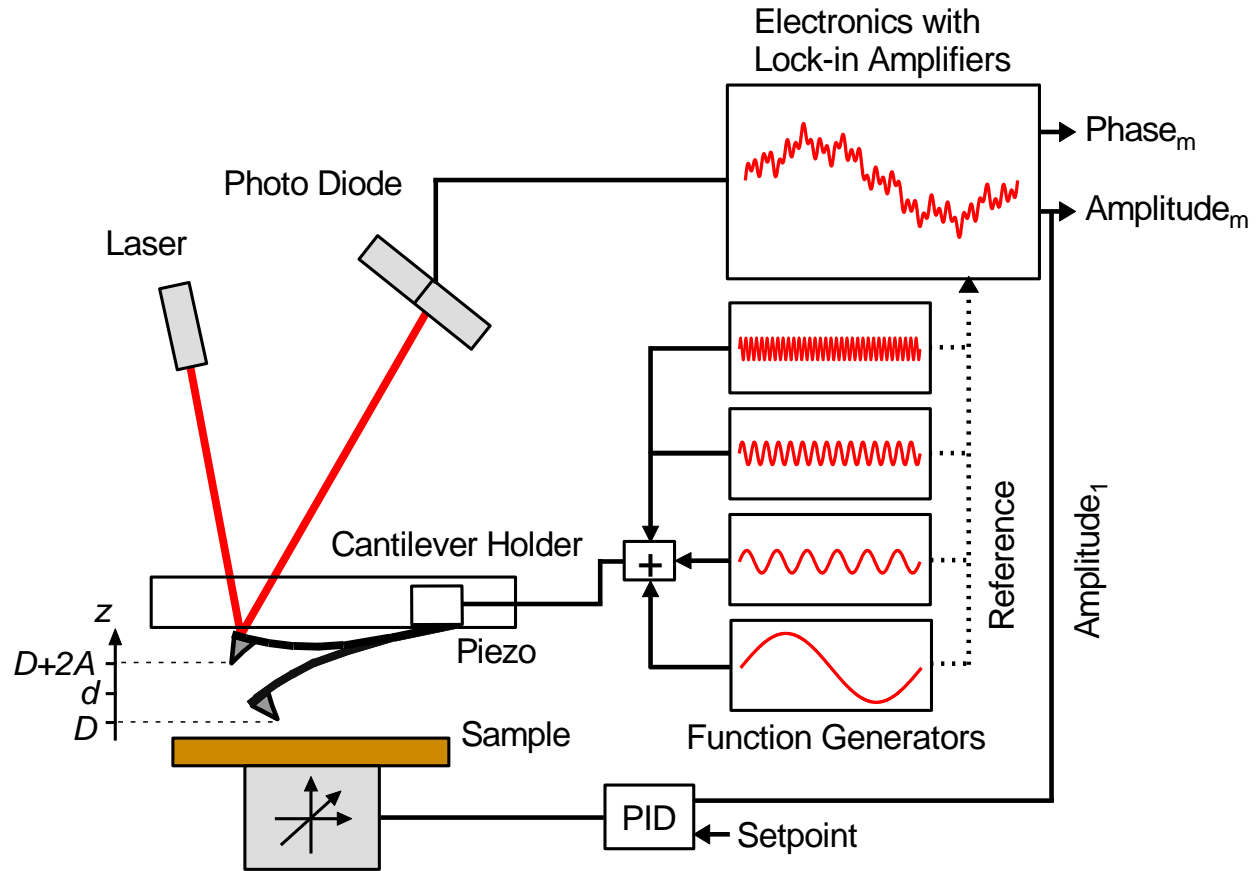


**Figure 1:** Schematic diagram of tetramodal AFM. The signals of four separate function generators are used to actively excite the cantilever at four different eigenmodes simultaneously. The signal of the tip trajectory measured by the photo diode is analyzed with four lock-in amplifiers, which provide the amplitude and phase values of each excited eigenmode separately and in real time. In our setup, an amplitude-modulation proportional-integral-derivative (PID) feedback loop controlled the first mode amplitude by adjusting the cantilever height above the surface, as is customary in tapping-mode AFM, while the other amplitudes were not controlled by the electronics. For pentamodal AFM the setup shown may be expanded with additional drive and lock-in electronics, accordingly. In principle, it is also possible to exchange parts of the driving electronics with phase-locked loops (PLLs) to drive certain eigenmodes in the frequency modulation scheme as in previous bimodal and trimodal applications [8, 20, 21].

## METHODS

### Experimental

We performed tetramodal (4-eigenmode) imaging experiments using a Cypher atomic force microscope (Asylum Research, Santa Barbara, CA), driving all four eigenmodes through the instrument's internal lock-ins. Since the number of signals that can be recorded with our instrument is limited to six, we only recorded the phase and amplitude of the second through fourth eigenmodes, which were most relevant to our study. Images were acquired with a resolution of  $512 \times 512$  pixels at a scan rate of 1 Hz in the fast direction. We used a commercial cantilever having its first four eigenfrequencies at approximately 76.4 kHz, 451.7 kHz, 1.21 MHz and 2.25 MHz, and a fundamental force constant of  $\approx 2$  N/m. The sample consisted of poly-tetrafluoroethylene (PTFE) pipe thread seal tape (nominal thickness  $\approx 0.1$  mm) stretched onto a hard plastic substrate, which was fixed on a metal substrate. This type of polymer sample was chosen in order to obtain high contrast in the phase signals. We carried out an extensive set of experiments varying the amplitude of each higher eigenmode in sequential images. In our baseline experiment we set the free fundamental amplitude to approximately 100 nm and the free amplitudes of eigenmodes 2 to 4 to approximately 2.9 nm, 1.8 nm and 1.3 nm, respectively, exciting each eigenmode at its measured eigenfrequency (the free amplitude is the oscillation amplitude for an eigenmode when the cantilever and sample are not engaged). We imaged the sample with an amplitude setpoint ratio of approximately 60 %, which led to stable characterization. The selected higher mode amplitudes correspond to a *photodetector* amplitude reading (in units of voltage) for each mode that is approximately 10 % of the value chosen for the fundamental free amplitude (this is due to the well-known differences in the optical

sensitivity factors for different modes [34]). We then acquired a series of images setting the amplitude of each higher eigenmode individually to 50 %, 200 %, 400 % and 800 % of the baseline amplitude, while keeping all other amplitudes constant, and scanning the same region of the sample (to avoid repetition we only show the most representative results). Finally, we calculated the average dissipated power ( $P_m$ ) and virial ( $V_m$ ) for each pixel of the images, for each eigenmode  $m$ , using the following expressions [32]:

$$P_m = \pi \frac{f_m k_m A_m^2}{Q_m} \left[ \frac{A_{free,m}}{A_m} \sin \phi_m - 1 \right] \quad (1)$$

$$V_m = \frac{k_m A_m}{2} \left[ -\frac{A_{free,m}}{Q_m} \cos \phi_m \right] \quad (2)$$

where  $P_m$  is defined here as power leaving mode  $m$  either to the tip-sample junction or as intermodal energy transfer (i.e., energy transferred from one mode to another). The other parameters are the drive frequency  $f$ , spring constant  $k$ , quality factor  $Q$ , amplitude  $A$ , and phase shift  $\phi$  of the corresponding mode  $m$ . Such definition implies that even when no net energy is dissipated irreversibly in the tip-sample junction,  $P_m$  might not be zero and a change in phase  $\phi_m$  might still arise. Mechanistically this can be understood by considering the average net power dissipated into the tip sample junction per cycle  $P_{dis}$  as the following sum:

$$P_{dis} = \sum_{m>0} P_m \quad (3)$$

Note that even when  $P_{dis} = 0$  in (3), the sines of the phase angles of the various modes ( $\sin \phi_m$ ) may still vary, which is the source of phase contrast when the tip-sample interaction is conservative. Furthermore, while the constraint  $E_{dis} \geq 0$  must apply for all modes considered together, for a given mode,  $P_m$  may be positive or negative depending on whether there is a net loss  $P_m < 0$  or gain  $P_m > 0$  in power *for that given mode* (in the results section it will be shown

that the sign of  $P_m$  depends on the free amplitude and amplitude setpoint ratio of the first mode, as well as on the free amplitudes of the higher modes).

The net tip-sample virial was calculated with a similar expression:

$$V = \sum_{m>0} V_m \quad (4)$$

Again, an interesting outcome of (4) is that even for zero net virial, i.e.,  $V = 0$ , contrast might arise in a given modal virial  $V_m$ . The sign of a given modal virial might also take positive or negative values. Such variations in the sign of the virial are illustrated in the results section and are shown to depend on the free amplitude and amplitude setpoint ratio of the first mode, as well as the higher mode amplitudes, similar to the dissipated power.

## Computational

For the numerical simulations five eigenmodes of the AFM cantilever were modeled using individual equations of motion for each, coupled through the tip-sample interaction forces similar to previous studies [16]. Driven eigenmodes were excited through a sinusoidal tip force of constant amplitude, and frequency equal to the natural frequency. The equations of motion were integrated numerically and the amplitude and phase of each eigenmode were calculated using the customary in-phase ( $I_i$ ) and quadrature ( $K_i$ ) terms:

$$I_m = \int_{N\tau_m} z_m(t) \cos(\omega_m t) dt \quad (5)$$

$$K_m = \int_{N\tau_m} z_m(t) \sin(\omega_m t) dt \quad (6)$$

where  $z_m(t)$  is the  $m$ -th eigenmode's spatial response in the time domain,  $N$  is the number of periods over which the phase and amplitude were averaged,  $\omega_m$  is its excitation frequency, and  $\tau_m$

is the *nominal* period of one oscillation.  $N$  was set to 25 for the fundamental eigenmode, and to the closest integer to 25 times  $\omega_m/\omega_1$  for the higher eigenmodes. The amplitude ( $A_m$ ) and phase ( $\phi_m$ ) were calculated, respectively, as:

$$A_m = \frac{\omega}{\pi N} \sqrt{I_m^2 + K_m^2} \quad (7)$$

$$\phi_m = \tan^{-1}(K_m / I_m) \quad (8)$$

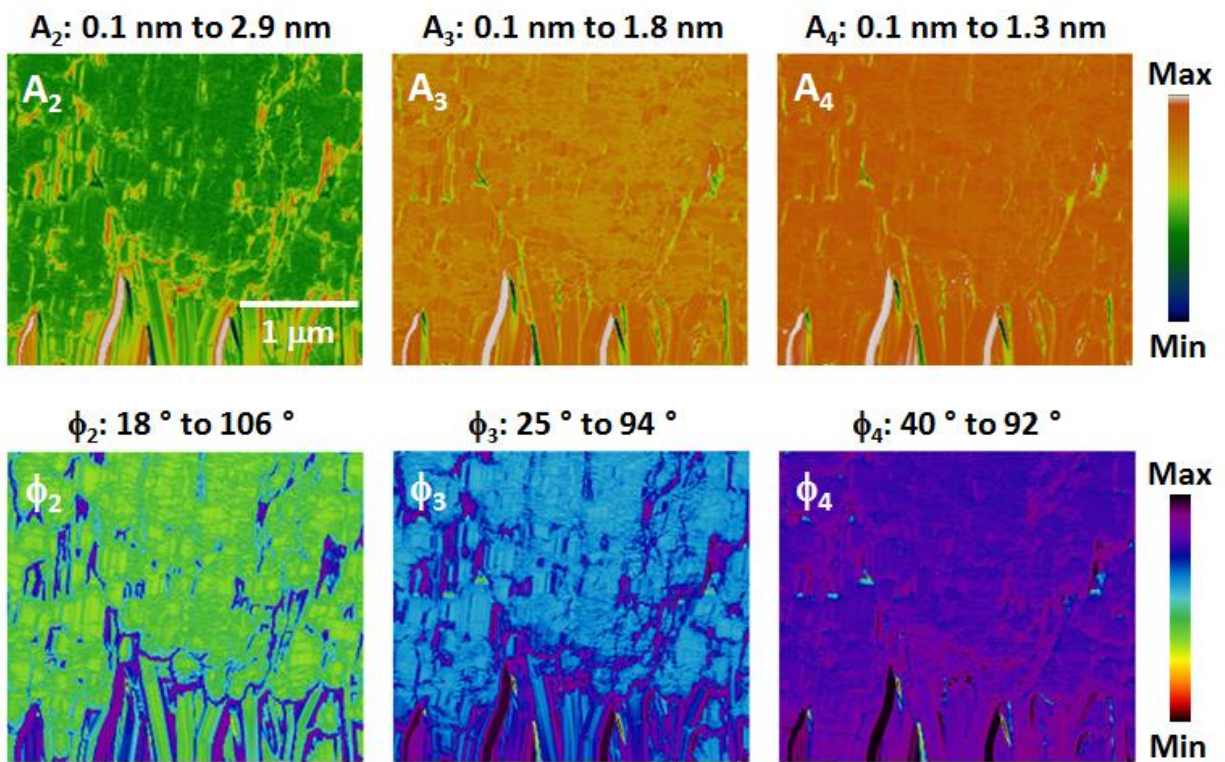
The repulsive tip-sample forces were accounted for through a standard linear solid (SLS) model [16] which exhibits both stress relaxation and creep. We used sample parameters typical of a polymer surface, with both linear springs having a stiffness of 7.5 N/m and the damper constant set to  $1 \times 10^{-5}$  Ns/m, similar to those of previous studies [16]. Long-range attractive interactions were included via the Hamaker equation [1] for a tip radius  $R$  of 10 nm and a Hamaker constant of  $2 \times 10^{-19}$  J.

Our computational results consisted of spectroscopy curves, where the cantilever approached the surface while we recorded the amplitudes and phases of all active eigenmodes, from which the respective average dissipated power and virial were calculated, as described in the experimental section. Here we also studied different free amplitudes for different eigenmodes (as with the experiments, only the most relevant results are shown).

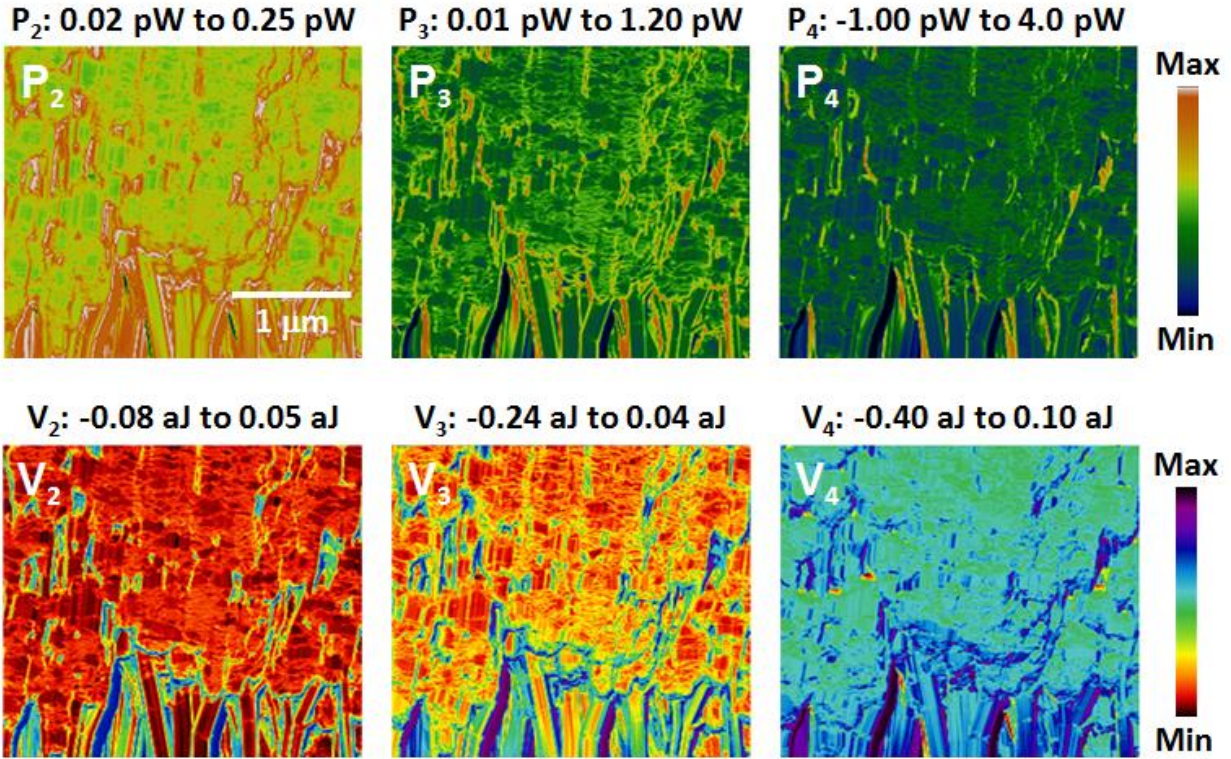
## RESULTS

Figure 2 shows the amplitude and phase images obtained for the higher eigenmodes (second to fourth modes) for the baseline experiment with  $A_{1-free} = 100$  nm,  $A_{2-free} = 2.9$  nm,  $A_{3-free} = 1.8$  nm, and  $A_{4-free} = 1.3$  nm and  $A_{setpoint} = 60$  %. The images reveal structures composed of highly oriented regions (towards the bottom of the images), along with amorphous regions showing globular morphology. The former are the result of stretching the PTFE film onto the

substrate and tend to dominate as the applied strain increases. During the acquisition of the images the first eigenmode remained in the repulsive imaging regime (with phase values below  $90^\circ$ ), although the higher eigenmodes exhibited phase values corresponding to the attractive regime (above  $90^\circ$ ) on some regions of the sample. Figure 3 shows the corresponding dissipated power and virial images, in which the contrast appears qualitatively sharper than in Figure 2. Notice in particular that the dissipated power image for the fourth eigenmode shows some negative values, indicating that this eigenmode received more energy than it dissipated at those pixels (see discussion below).



**Figure 2.** Experimental baseline amplitude (top row) and phase (bottom row) measurements performed on the PTFE sample for the higher eigenmodes using  $A_{1-free} = 100$  nm,  $A_{2-free} = 2.9$  nm,  $A_{3-free} = 1.8$  nm,  $A_{4-free} = 1.3$  nm and  $A_{setpoint} = 60$  %.



**Figure 3.** Calculated average dissipated power (top row) and virial (bottom row) for the experimental images of Figure 2 using the expressions provided in the experimental methods section.

Figure 4 shows higher eigenmode dissipation images similar to those of Figure 3, but for different amplitude of the third eigenmode (middle column), which had successive values (from top to bottom) of approximately 0.9 nm, 3.6 nm, 7.2 nm and 14.4 nm. As the results show, the range of dissipated power remained nearly constant for the eigenmodes for which the amplitude did not vary. Specifically, for the second eigenmode, the respective 1-standard-deviation intervals were  $0.13 \text{ pW} \pm 0.04 \text{ pW}$ ,  $0.15 \text{ pW} \pm 0.18 \text{ pW}$ ,  $0.16 \text{ pW} \pm 0.04 \text{ pW}$  and  $0.17 \text{ pW} \pm 0.04 \text{ pW}$ , corresponding to the images in the left column of Figure 4. Similarly, the respective intervals for the fourth eigenmode (right column of Figure 4) were  $0.87 \text{ pW} \pm 0.65 \text{ pW}$ ,  $0.66 \text{ pW}$

$\pm 0.57$  pW,  $0.34$  pW  $\pm 0.60$  pW and  $0.16$  pW  $\pm 0.63$  pW. The average dissipated power in the above intervals shows a very slight upward trend for the second mode and a slight downward trend for the fourth mode. In contrast, the range of dissipated power was significantly larger for the third eigenmode (middle column in Figure 4) as its free amplitude increased and the average values exhibited greater variation. The corresponding intervals were  $-0.19$  pW  $\pm 0.10$  pW,  $-1.62$  pW  $\pm 1.41$  pW,  $-2.42$  pW  $\pm 4.98$  pW, and  $-5.45$  pW  $\pm 16.58$  pW. Additionally, as the third free amplitude increased, the range of *negative* power values also increased (the corresponding lower limit of the dissipated power images for this eigenmode was  $-0.4$  pW,  $-5.3$  pW,  $-11.1$  pW and  $-13.0$  pW), suggesting that greater intermodal energy transfer took place (see discussion).

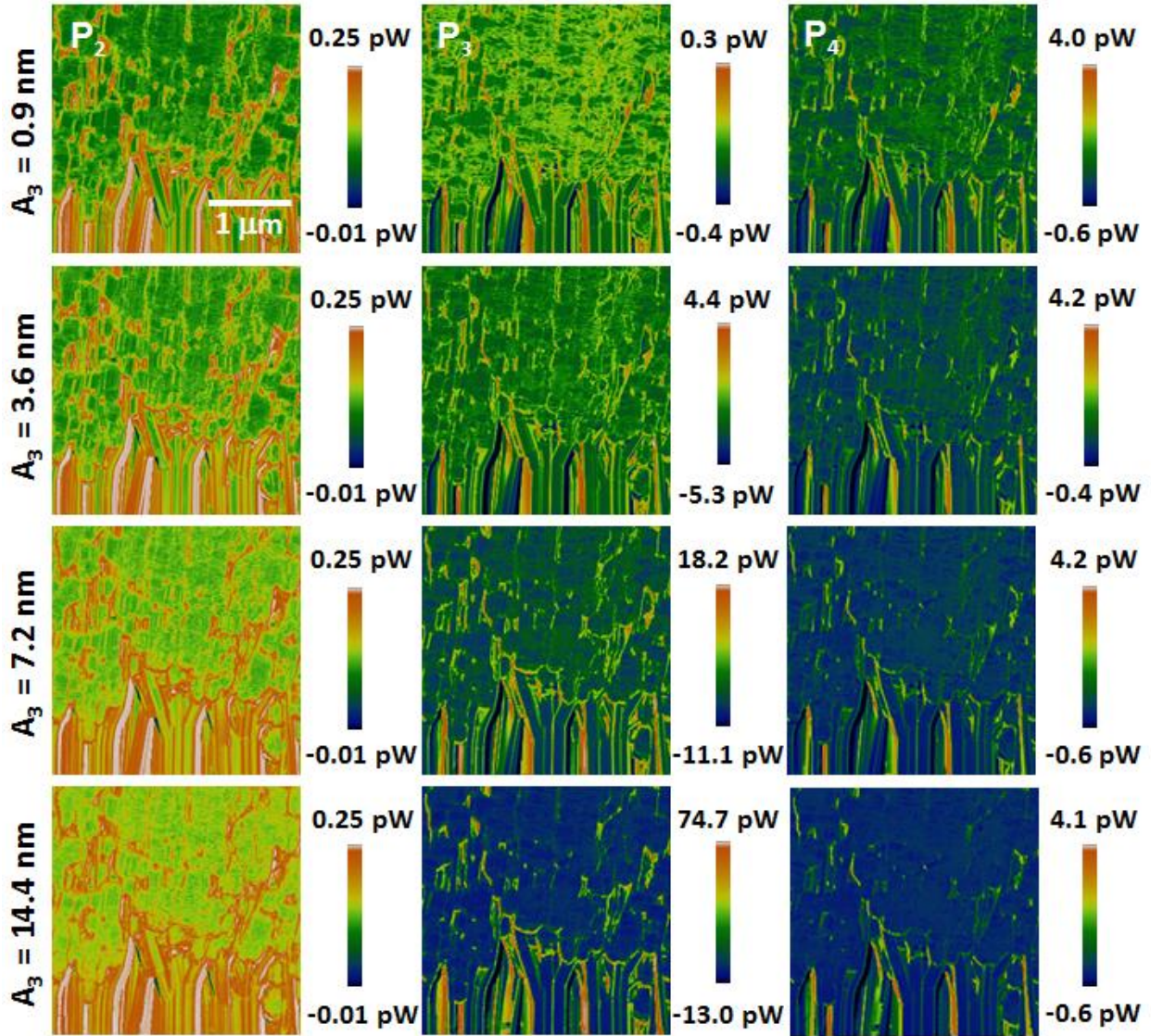


**Figure 4.** Calculated dissipated power images for the higher eigenmodes for experimental images similar to those of Figure 2, but for increasing third eigenmode amplitude (the three columns of the image show the results for the second, third and fourth eigenmode, respectively). The free amplitudes of the first, second and fourth eigenmodes, as well as the amplitude setpoint ratio are the same as listed for Figure 2.

Figure 5 shows the corresponding virial images for Figure 4. As the results show, the range of the virial remained nearly constant for the eigenmodes for which the amplitude did not

vary (similar to the power images), but became larger for the third eigenmode as its amplitude increased. The 1-standard-deviation intervals for the second eigenmode (left column in Figure 5) were (from top to bottom)  $-0.05 \text{ aJ} \pm 0.02 \text{ aJ}$ ,  $-0.06 \text{ aJ} \pm 0.02 \text{ aJ}$ ,  $-0.06 \text{ aJ} \pm 0.023 \text{ aJ}$  and  $-0.06 \text{ aJ} \pm 0.03 \text{ aJ}$ . The corresponding intervals for the third eigenmode (middle column in Figure 5) were  $-0.04 \text{ aJ} \pm 0.02 \text{ aJ}$ ,  $-0.57 \text{ aJ} \pm 0.23 \text{ aJ}$ ,  $-1.50 \pm 0.50 \text{ aJ}$  and  $-2.70 \pm 1.17 \text{ aJ}$ . Finally, the intervals for the fourth eigenmode were  $-0.14 \text{ aJ} \pm 0.06 \text{ aJ}$ ,  $-0.10 \text{ aJ} \pm 0.05 \text{ aJ}$ ,  $-0.07 \text{ aJ} \pm 0.04 \text{ aJ}$  and  $-0.05 \text{ aJ} \pm 0.04 \text{ aJ}$ . Overall, the third mode virial became more negative for higher amplitudes, in agreement with previous studies indicating that greater amplitudes lead to greater penetration into the sample, which in turn result in greater repulsive forces [16]. Despite the nearly constant range of values for the virial of eigenmodes 2 and 4, the results show that their respective images are influenced by changes in the amplitude of the third eigenmode: as the third amplitude increases, a gradual overall trend towards lower values is observed for the second virial, while the fourth virial trends towards higher values.

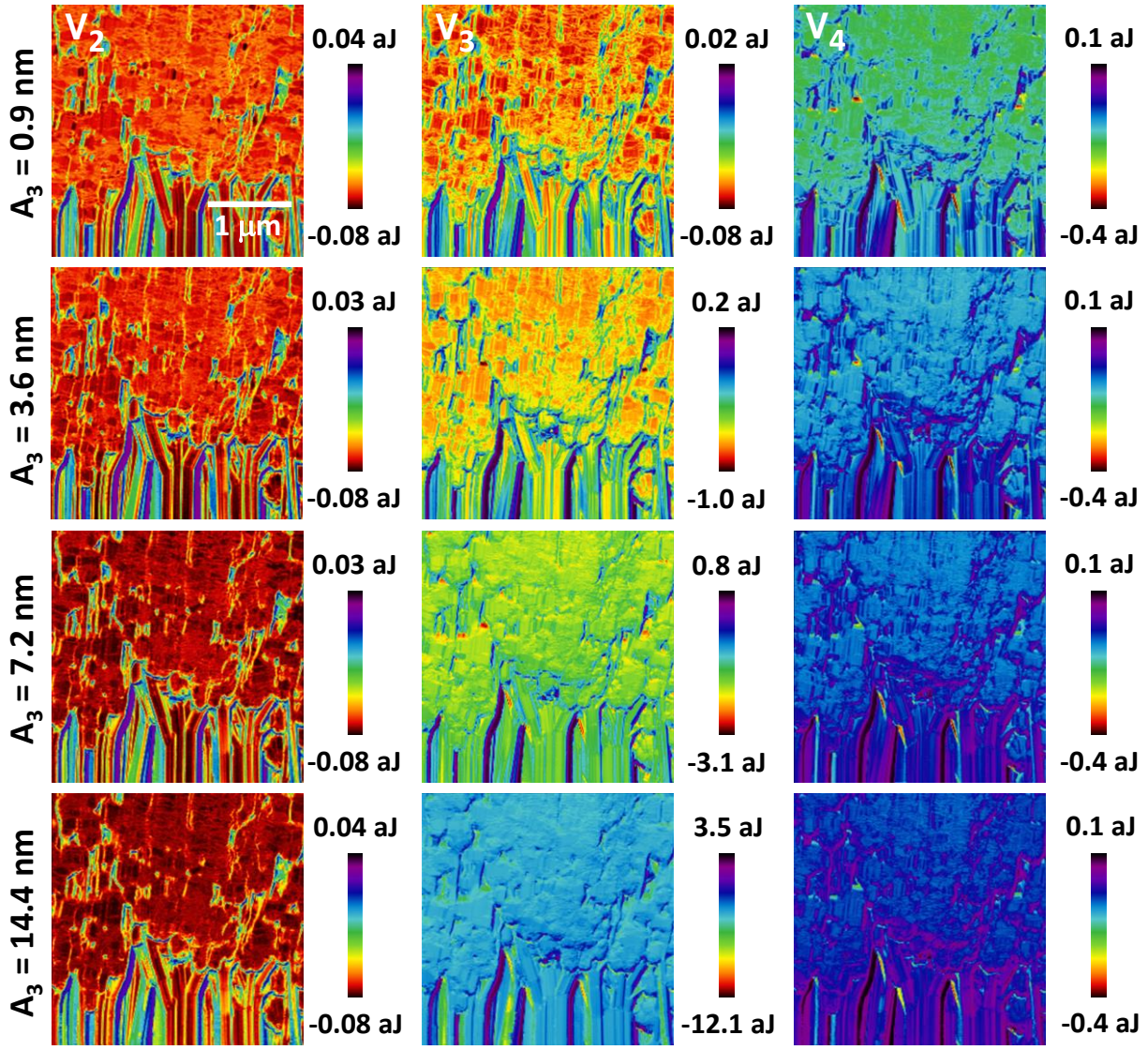


**Figure 5.** Calculated virial images for the higher eigenmodes for experimental images similar to those of Figure 2, but for increasing third eigenmode amplitude (as in Figure 4, the three columns of the image show the results for the second, third and fourth eigenmodes, respectively). The amplitudes of the first, second and fourth eigenmodes, as well as the amplitude setpoint ratio are the same as listed for Figure 2.

Figures 6 and 7 show computational results of pentamodal spectroscopy curves for different ratios of the higher mode amplitude to the fundamental mode amplitude. In Figure 6

this ratio is 1:100 (the higher mode free amplitudes are each 1 % of the fundamental free amplitude) and in Figure 7 it is 3:80 (the higher mode free amplitudes are each 3.75 % of the fundamental free amplitude). Interestingly, significant differences emerge with such a small change in the higher mode amplitude ratio. When the amplitude ratio is 1:100, the behavior of the dissipated power as a function of the cantilever height is similar for different eigenmodes. The power increases as the cantilever first reaches the sample, and then decreases as the cantilever gets very close. Additionally, the dissipated power is in general positive for all eigenmodes, indicating that they all lose energy as the tip interacts with the surface (see Figure 6a). However, for the larger amplitude ratio of 3:80 the trends in dissipated power vs. cantilever height seem erratic and include negative values, indicating that energy is transferred into some of the eigenmodes for certain cantilever heights (see Figure 7a). In contrast, the total dissipated power for all eigenmodes *combined* exhibits the expected trend for both simulations (see Figures 6c and 7c). In Figure 6b and 7b the dissipated power curves for individual eigenmodes (see Figure 6a and 7a) were added up consecutively (that is, the curve for each eigenmode includes the contribution of all lower eigenmodes). In this type of representation the contribution of each individual eigenmode to the total dissipated power becomes more obvious by considering the colored area enclosed between each set of two curves. For the smaller amplitude ratio of 1:100 the dissipated power is very low for the 2<sup>nd</sup> eigenmode (the area between red and blue curve is almost not discernible) and increases with each subsequent eigenmode. For the larger amplitude ratio of 3:80 the individual contributions have changed dramatically, increasing and decreasing, due the large energy transfer between eigenmodes. Finally, the trend in the virial for both sets of simulations (Figures 6d and 7d) transitions from a curve that exhibits a minimum for the lowest eigenmodes into a monotonic curve of positive slope for higher eigenmodes. Our simulations

also show that the curve for higher eigenmodes undergoes a similar transition (from concave upward with a minimum to monotonic with positive slope) as that eigenmode's amplitude increases (not shown). In general, the selection of a small free amplitude value for a given eigenmode favors a curve that is concave upwards and contains a minimum, while the use of a large free amplitude value favors a monotonic curve that has positive slope and does not contain a minimum.

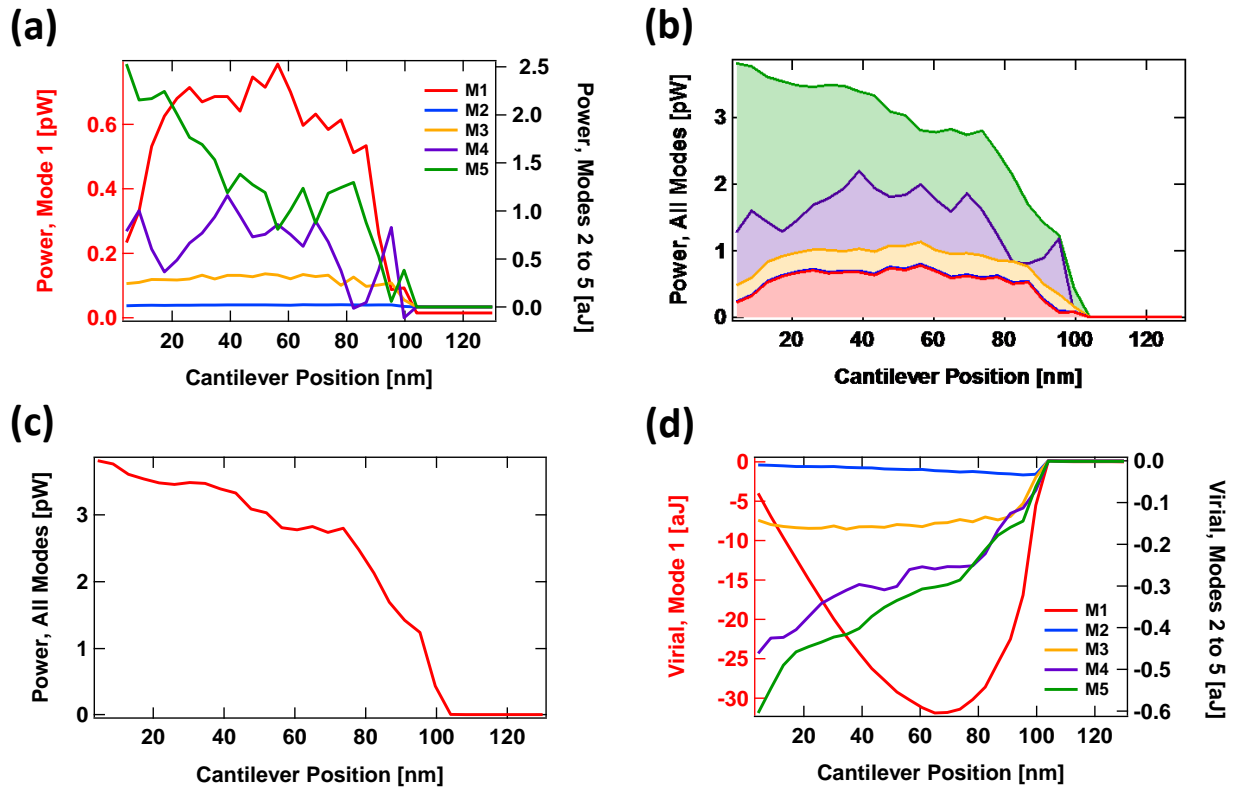


**Figure 6.** Simulations of dissipated power and virial for pentamodal spectroscopy curves using higher to lower mode free amplitude ratios of 1:100 (1 %): (a) dissipated power for individual eigenmodes; (b) incremental dissipated power (the curve for each eigenmode includes the contribution of all lower eigenmodes); (c) total dissipated power including all eigenmodes; (d) virial for individual eigenmodes. Note that the data for the fundamental eigenmode is plotted using the left axis, while the data for modes 2 to 5 is plotted using the right axis in panels (a) and

(d). For this calculation we used  $A_{1-free} = 100$  nm,  $A_{2-free} = A_{3-free} = A_{4-free} = A_{5-free} = 1$  nm and modeled a cantilever similar to the one used in the experiments.

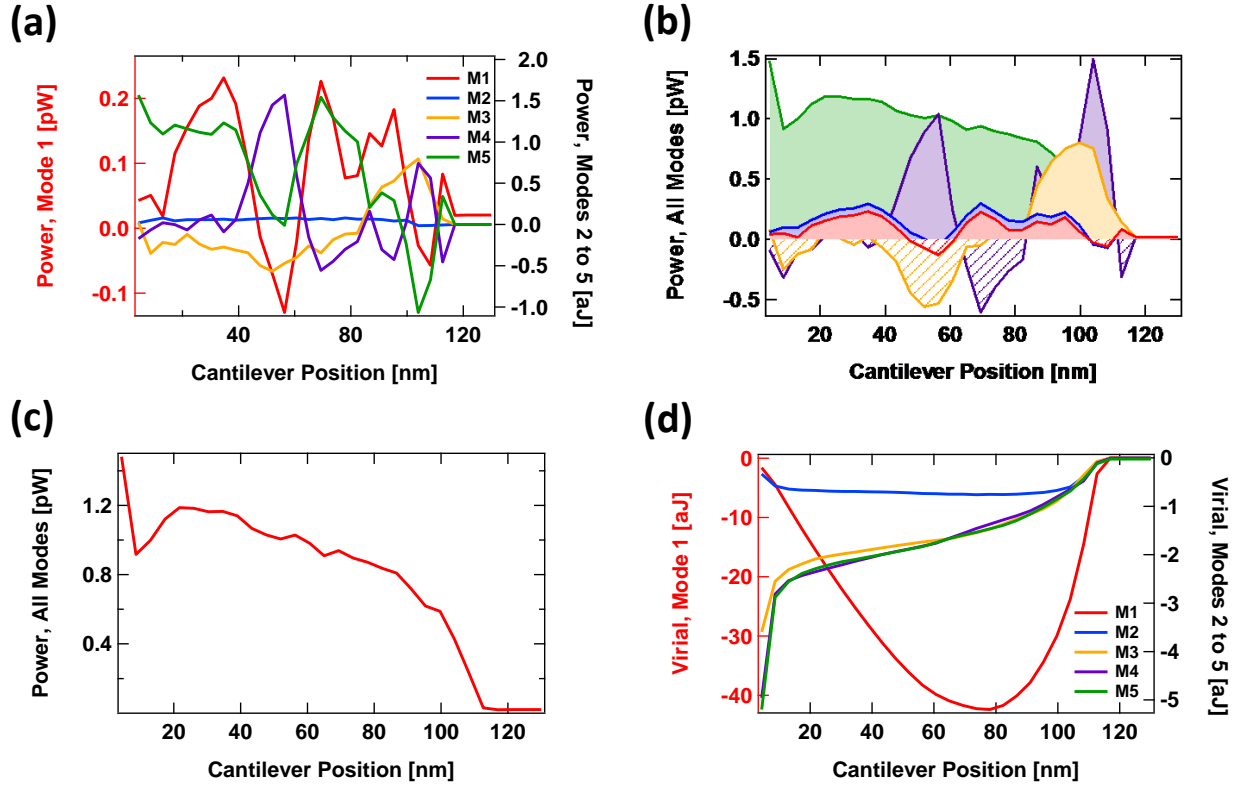


**Figure 7.** Simulations of dissipated power and virial for pentamodal spectroscopy curves using higher to lower mode amplitude ratios of 3:80 (3.75 %): (a) dissipated power for individual eigenmodes; (b) incremental dissipated power (the curve for each eigenmode includes the contribution of all lower eigenmodes); (c) total dissipated power including all eigenmodes; (d) virial for individual eigenmodes. Note that the data for the fundamental eigenmode is plotted using the left axis, while the data for modes 2 to 5 is plotted using the right axis in panels (a) and (d).

(d). For this calculation we used  $A_{1-free} = 80$  nm,  $A_{2-free} = A_{3-free} = A_{4-free} = A_{5-free} = 3$  nm and modeled a cantilever similar to the one used in the experiments.

## DISCUSSION

The first important detail to note from Figures 2 and 3, and in particular in the context of multimodal AFM, is the degree to which the contrast channels are relevant and meaningful. Figure 2 shows direct experimental observables (amplitudes and phases), whereas Figure 3 shows the physical phenomena that induce the contrast in the observables (dissipated power or energy transfer and virial). Arguably the latter are physically more intuitive and can be employed, even by visual inspection, to interpret image contrast to a great extent (recall that despite their meaningfulness, these quantities are averages so they still do not fully capture the richness of multifrequency impacts [16]). For example, in Figure 2 the contrast could be argued to decrease in both amplitude  $A$  and phase  $\phi$  with increasing eigenmode order or frequency. However, the calculated dissipated power and virial exhibit greater contrast. For the amplitude and phase images, the ratio of the standard deviation to the range of values observed in the images was on average approximately 8 % and 10 %, respectively, whereas it was approximately 15 % and 17 % for the dissipated power and virial, respectively. The practical outcome from an experimental point of view is as follows: what could be perceived as small contrast by inspection of observables in higher eigenmode channels could in fact be translated into large contrast in terms of the physical quantities that involve energy. This discrepancy could be qualitatively understood by analyzing the way in which observables (phase and amplitude) scale relative to physical derivatives, which scale with spring constant and Q factor.

Secondly, within monomodal amplitude modulation AFM, the phase contrast obtained from the single (fundamental) externally excited mode, is typically related to irreversible losses of energy in the tip-sample junction [30] and can be related to several phenomenological nanoscale mechanisms [35]. Energy dissipation in multifrequency AFM, however, is a topic that

is still under investigation by several groups [36-39] and the origin of contrast in both the amplitude and phase channels may be more closely related to the dynamics of single mode AFM in low- $Q$  environments [40] in the context of energy transfer between harmonics and modes [41]. A crucial difference, however, is to be noted. Under single-mode external excitation, energy or power dissipation ( $P_m$ ) cannot be negative at the first mode and has to be negative at all other frequencies. This is because energy flows from the first (excited mode) to all other higher frequencies. On the other hand, equation (3) implies that by introducing energy at several frequencies or eigenmodes, power transfer may be negative or positive for a given mode without compromising the net power dissipation  $P_{dis} \geq 0$ . We believe that this critical difference between monomodal and multimodal AFM is the cause of the negative values of  $P_m$  observed in our computational and experimental results.

Thirdly, Figures 4 and 5 show how the ranges in power  $P_m$  and  $V_m$  (particularly from mode 3 in the images) increase with increasing modal free amplitude. To a first approximation this could be related to the kinetic energy ratios as it has been recently argued [37, 42]. However, a qualitative interpretation could be also given by combining (1) and (2) as follows:

$$\frac{1}{2}k_m A_m A_r A_{free,m} = -V_m Q_m \tan \phi_m - \frac{P_m Q_m}{2\pi} \quad (9)$$

Here the term on the left is the kinetic energy of mode  $m$  and  $A_r$  is simply the amplitude ratio  $A_m/A_{free,m}$ . We see that the physical derivatives  $V_m$  and  $P_m$  scale with  $A_{free,m}$  in equation (9), in qualitative agreement with Figures 4 and 5. Note also that for the other modes, where the free amplitude has been left constant, the ranges of the physical derivatives do not vary appreciably. A similar analysis can be carried out to explain the overall increase in the magnitude of  $V_m$  and  $P_m$  with increasing mode order (not shown), although variations to these general trends are also observed in the data.

Our simulations suggest that the relative ratios between free amplitudes also need to be considered. In particular, 1:100 and 3:80 has been employed in Figures 6 and 7 respectively, although the results suggest that the fluctuations in dissipated power between positive and negative values are a general phenomenon that becomes more prevalent as the tip-sample impact becomes more irregular, which is the case in a multimodal oscillation when the higher mode amplitudes are increased. A comparison of contributions from individual eigenmodes to the total dissipated power, similar to the comparison shown in Figures 6b and 7b, should be interesting for follow-up experimental work on sample systems with different material properties. As the proportion of the single-mode contributions depends on the energy transfer between the corresponding eigenmodes, the observed energy derivatives should be highly sensitive to differences in viscoelasticity between different regions of the sample. In particular, changes in relaxation time(s) should lead to a shift of dissipated power into eigenmodes with higher or lower frequencies. Admittedly, one would expect this redistribution of energy to also be affected by other factors, such as the complex dynamics of the cantilever or the indentation depth. Nevertheless, the proposed method could provide a means to qualitatively analyze frequency dependent responses across the sample.

In closing this section, we remind the reader that the complex nature of the tip-sample impact in multifrequency AFM, whereby each impact is the result of a trajectory involving multiple sinusoidal oscillations of different frequencies and where individual impacts for different cycles of the fundamental eigenmode can differ from one another, can prevent the tip motion from reaching steady state, even when this may not be obvious to the user [43]. This unsteady behavior, which becomes more prevalent as more eigenmodes are turned on, can affect the stability of the amplitude-modulation control loop, leading to cross-talk between the

topography and the material contrast images [43]. In such cases, the observed contrast may not be completely due to variations in the properties of the sample, but may be partially due to unsteady tip oscillations. It is therefore important during an experiment to monitor the signals and select scan speeds and parameters that minimize the fluctuations in the fundamental mode amplitude when the cantilever and sample are engaged. Finally, we also remind the reader that, in general, the use of higher eigenmodes leads to greater penetration of the tip into the sample, which can in some cases compromise the integrity of the tip due to increased contamination and/or greater mechanical damage with respect to the single-eigenmode case [16].

## **CONCLUSIONS**

We have conducted experimental and computational investigations of tetramodal and pentamodal atomic force microscopy (AFM), illustrating the acquisition of six to eight additional observables (amplitude and phase signals), with respect to single-eigenmode tapping-mode AFM. We have showed that the dissipation and virial expressions for the respective eigenmodes provide enhanced and more physically meaningful information than the amplitudes and phases, and highlight hidden phenomena such as intermodal energy transfer. We believe that multimodal imaging could provide the means to carry out more statistically robust spectroscopy, whereby information from different eigenmodes is complementary, as well as frequency dependent characterization of surfaces whose material properties exhibit multiple relaxation times that vary across the surface.

## **ACKNOWLEDGEMENT**

SA acknowledges the Basic Science Research Program through the National Research Foundation of Korea (NRF), funded by the Ministry of Education, Science and Technology (Grant No. 2013R1A6A3A03063900) and the Cooperative Research Agreement between the University of Maryland and the National Institute of Standards and Technology Center for Nanoscale Science and Technology, award 70NANB10H193, through the University of Maryland. SDS acknowledges support from National Institute of Standards and Technology Center for Nanoscale Science and Technology, through intergovernmental personnel assignment award IP1304.

## **DISCLAIMER**

Certain commercial equipment, instruments or materials are identified in this document. Such identification does not imply recommendation or endorsement by the National Institute of Standards and Technology, nor does it imply that the products identified are necessarily the best available for our purposes.

## REFERENCES

- [1] Garcia, R., and Perez, R., 2002, "Dynamic atomic force microscopy methods," *Surf. Sci. Rep.*, 47, pp. 197-301.
- [2] Giessibl, F. J., 2003, "Advances in atomic force microscopy," *Rev. Modern Phys.*, 75(3), pp. 949-983.
- [3] Rodriguez, T., and Garcia, R., 2004, "Compositional mapping of surfaces in atomic force microscopy by excitation of the second normal mode of the microcantilever," *Appl. Phys. Lett.*, 84, pp. 449-451.
- [4] Sahin, O., Magonov, S., Su, C., Quate, C. F., and Solgaard, O., 2007, "An atomic force microscope tip designed to measure time-varying nanomechanical forces," *Nature Nanotech.*, 2, pp. 507-514.
- [5] Raman, A., Trigueros, S., Cartagena, A., Stevenson, A. P. Z., Susilo, M., Nauman, E., and Contera, S. A., 2011, "Mapping nanomechanical properties of live cells using multi-harmonic atomic force microscopy," *Nature Nanotech.*, 6, pp. 809-814.
- [6] Parot, P., Dufrene, Y. F., Hinterdorfer, P., Grimellec, C. L., Navajas, D., Pellequer, J. L., and Scheuring, S., 2007, "Past, present and future of atomic force microscopy in life sciences and medicine," *J. Mol. Recog.*, 20, pp. 418-431.
- [7] Platz, D., Forchheimer, D., Tholen, E., and Haviland, D. B., 2013, "Interaction imaging with amplitude-dependence force spectroscopy," *Nature Comm.*, 4, p. 1360.
- [8] Herruzo, E. T., Perrino, A. P., and Garcia, R., 2014, "Fast nanomechanical spectroscopy of soft matter," *Nature Comm.*, 5, p. No. 3126.
- [9] Butt, H. J., Cappella, B., and Kappl, M., 2005, "Force measurements with the atomic force microscope: Technique, interpretation and applications," *Surf. Sci. Rep.*, 59, pp. 1-152.
- [10] Piner, R. D., Zhu, J., Xu, F., Hong, S., and Mirkin, A. C., 1999, "'Dip-Pen' Nanolithography," *Science*, 283, pp. 661-663.
- [11] Martinez, N. F., Lozano, J., Herruzo, E. T., Garcia, F., Richter, C., Sulzbach, T., and Garcia, R., 2008, "Bimodal atomic force microscopy imaging of isolated antibodies in air and liquids," *Nanotechnology*, 19, p. 384011.
- [12] Herruzo, E. T., Asakawa, H., Fukuma, T., and Garcia, R., 2013, "Three-dimensional quantitative force maps in liquid with 10 piconewton, angstrom and sub-minute resolutions," *Nanoscale*, 5, pp. 2678-2685.
- [13] Legleiter, J., Park, M., Cusick, B., and Kowalewski, T., 2006, "Scanning probe acceleration microscopy (SPAM) in fluids: mapping mechanical properties of surfaces at the nanoscale," *Proc. Natl. Acad. Sci. USA*, 103, pp. 4813-4818.
- [14] Guo, S., Solares, S. D., Mochalin, V., Neitzel, I., Gogotsi, Y., Kalinin, S. V., and Jesse, S., 2012, "Multifrequency imaging in the intermittent contact mode of atomic force microscopy: beyond phase imaging," *Small*, 8, pp. 1264-1269.
- [15] Tetard, L., Passian, A., and Thundat, T., 2009, "New modes for subsurface atomic force microscopy through nanomechanical coupling," *Nature Nanotech.*, 5, pp. 105-109.
- [16] Ebeling, D., Eslami, B., and Solares, S. D., 2013, "Visualizing the subsurface of soft matter: simultaneous topographical imaging, depth modulation and compositional mapping with triple frequency atomic force microscopy," *ACS Nano*, 7, pp. 10387-10396.

- [17] Stan, G., Solares, S. D., Pittenger, B., Erina, N., and Su, C., 2014, "Nanoscale mechanics by tomographic contact resonance atomic force microscopy," *Nanoscale*, 6(2), pp. 962-969.
- [18] Garcia, R., and Proksch, R., 2013, "Nanomechanical mapping of soft matter by bimodal force microscopy," *European Pol. J.*, 49, pp. 1897-1906.
- [19] Ebeling, D., and Solares, S. D., 2013, "Amplitude modulation dynamic force microscopy imaging in liquids with atomic resolution: comparison of phase contrasts in single and dual mode operation," *Nanotechnology*, 24, p. No. 135702.
- [20] Chawla, G., and Solares, S. D., 2011, "Mapping of conservative and dissipative interactions in bimodal atomic force microscopy using open-loop and phase-locked-loop control of the higher eigenmode," *Applied Physics Letters*, 99(7).
- [21] Solares, S. D., and Chawla, G., 2010, "Triple-frequency intermittent contact atomic force microscopy characterization: Simultaneous topographical, phase, and frequency shift contrast in ambient air," *J. Appl. Phys.*, 108, p. 054901.
- [22] Jesse, S., Kalinin, S., Proksch, R., Baddorf, A., and Rodriguez, B., 2007, "The band excitation method in scanning probe microscopy for rapid mapping of energy dissipation on the nanoscale," *Nanotechnology*, 18, p. 435503.
- [23] Kareem, A. U., and Solares, S. D., 2012, "Characterization of surface stiffness and probe-sample dissipation using the band excitation method of atomic force microscopy: a numerical analysis," *Nanotechnology*, 23, p. 015706.
- [24] Stark, M., Stark, R. W., Heckl, W. M., and Guckenberger, R., 2002, "Inverting dynamic force microscopy: From signals to time-resolved interaction forces," *Proc. Natl. Acad. Sci. USA*, 99, pp. 8473-8478.
- [25] Solares, S. D., and Holscher, H., 2010, "Numerical analysis of dynamic force spectroscopy using the torsional harmonic cantilever," *Nanotechnology*, 21, p. 075702.
- [26] Platz, D., Tholen, E. A., Pesen, D., and Haviland, D. B., 2008, "Intermodulation atomic force microscopy," *Appl. Phys. Lett.*, 92, p. 153106.
- [27] Borysov, S. S., Platz, D., de Wijn, A. S., Forchheimer, D., Tolen, E. A., Balatsky, A. V., and Haviland, D. B., 2013, "Reconstruction of tip-surface interactions with multimodal intermodulation atomic force microscopy," *Phys. Rev. B*, 88, p. 115405.
- [28] Rodriguez, B. J., Callahan, C., Kalinin, S. V., and Proksch, R., 2007, "Dual-frequency resonance-tracking atomic force microscopy," *Nanotechnology*, 18, p. 475504.
- [29] Killgore, J. P., Yablon, D. G., Tsou, A. H., Gannepalli, A., Yuya, P. A., Turner, J. A., Proksch, R., and Hurley, D. C., 2011, "Viscoelastic Property Mapping with Contact Resonance Force Microscopy," *Langmuir*, 27, pp. 13983-13987.
- [30] Cleveland, J. P., Anczykowski, B., Schmid, A. E., and Elings, V. B., 1998, "Energy dissipation in tapping-mode atomic force microscopy," *Appl. Phys. Lett.*, 72, pp. 2613-2615.
- [31] Garcia, R., Tamayo, J., and San Paulo, A., 1999, "Phase contrast and surface energy hysteresis in tapping mode scanning force microscopy," *Surf. Interf. Anal.*, 27, pp. 312-316.
- [32] Lozano, J. R., and Garcia, R., 2008, "Theory of multifrequency atomic force microscopy," *Phys. Rev. Lett.*, 100, p. 076102.
- [33] Lozano, J., and Garcia, R., 2009, "Theory of phase spectroscopy in bimodal atomic force microscopy," *Phys. Rev. B*, 79, p. 014110.

- [34] Garcia, R., and Herruzo, E. T., 2012, "The emergence of multifrequency atomic force microscopy," *Nature Nanotech.*, 4, pp. 217-226.
- [35] Garcia, R., Gómez, C. G., Martínez, N. F., Patil, S., Dietz, C., and Magerle, R., 2006, "Identification of Nanoscale Dissipation Processes by Dynamic Atomic Force Microscopy," *Phys. Rev. Lett.*, 97, p. 016103.
- [36] Pukhova, V., Banfi, F., and Ferrini, G., 2014, "Energy dissipation in multifrequency atomic force microscopy," *Beilstein J. Nanotech.*, 5, pp. 494–500.
- [37] Chakraborty, I., and Yablon, D., 2013, "Cantilever energy effects in bimodal AFM: phase and amplitude contrast of multicomponent samples," *Nanotechnology*, 24, p. No. 475706.
- [38] Santos, S., Gadelrab, K. R., Barcons, V., Font, J., Stefancich, M., and Chiesa, M., 2012, "The additive effect of harmonics on conservative and dissipative interactions," *J. Appl. Phys.*, 112, p. 124901.
- [39] Santos, S., 2014, "Phase contrast and operation regimes in multifrequency atomic force microscopy," *Appl. Phys. Lett.*, 104, p. 143109.
- [40] Melcher, J., Carrasco, C., Xu, X., Carrascosa, J. L., Gomez-Herrero, J., de Pablo, P. J., and Raman, A., 2009, "Origins of phase contrast in the atomic force microscope in liquids," *Proc. Natl. Acad. Sci. USA*, 106, pp. 13655-13660.
- [41] Payam, A. F., Ramos, J. R., and Garcia, R., 2012, "Molecular and Nanoscale Compositional Contrast of Soft Matter in Liquid: Interplay between Elastic and Dissipative Interactions," *ACS Nano*, 6, pp. 4663–4670.
- [42] Yablon, D. G., Grabowski, J., and Chakraborty, I., 2014, "Measuring the loss tangent of polymer materials with atomic force microscopy based methods," *Meas. Sci. & Technol.*, 25, p. 055402.
- [43] Solares, S. D., and Chawla, G., 2010, "Frequency response of higher cantilever eigenmodes in bimodal and trimodal tapping mode atomic force microscopy," *Measurement Science & Technology*, 21(12).